

A study of 10 Rotating Radio Transients using Parkes radio telescope

Xinhui Ren^{1,2,3}, Jingbo Wang³, Wenming Yan^{1,4}, Jintao Xie⁵, Shuangqiang Wang¹, Yirong Wen^{1,2,3}, Yong Xia^{1,2,3}

¹ Xinjiang Astronomical Observatory, Chinese Academy of Sciences, Urumqi, Xinjiang 830011, People's Republic of China

² University of Chinese Academy of Sciences, Beijing 100049, People's Republic of China

³ Institute of Optoelectronic Technology, Lishui University, Lishui, Zhejiang, 323000, People's Republic of China; 1983wangjingbo@163.com

⁴ Xinjiang Key Laboratory of Radio Astrophysics, Urumqi, Xinjiang, 830011, People's Republic of China

⁵ Research Center for Intelligent Computing Platforms, Zhejiang Laboratory, Hangzhou, Zhejiang 311100, China

Received 20XX Month Day; accepted 20XX Month Day

Abstract Rotating Radio Transients (RRATs) are a relatively new subclass of pulsars that emit detectable radio bursts sporadically. We conducted an analysis of 10 RRATs observed using the Parkes telescope, with 8 of these observed via the Ultra-Wideband Receiver. We measured the burst rate and produced integrated profiles spanning multiple frequency bands for 3 RRATs. We also conducted a spectral analysis on both integrated pulses and individual pulses of 3 RRATs. All of their integrated pulses follow a simple power law, consistent with the known range of pulsar spectral indices. Their average spectral indices of single pulses are -0.9, -1.2, and -1.0 respectively, which are within the known range of pulsar spectral indices. Additionally, we find that the spreads of single-pulse spectral indices for these RRATs (ranging from -3.5 to +0.5) are narrower compared to what has been observed in other RRATs (Shapiro-Albert et al. 2018; Xie et al. 2022). It is notable that the average spectral index and scatter of single pulses are both relatively small. For the remaining 5 RRATs observed at the UWL receiver, we also provided the upper limits on fluence and flux density. In addition, we obtained the timing solution of PSR J1709-43. Our analysis shows that PSRs J1919+1745, J1709-43 and J1649-4653 are potentially nulling pulsars or weak pulsars with sparse strong pulses.

1 INTRODUCTION

Pulsars serve as the cosmic lighthouses and can be a powerful tool for numerous astronomical studies. They are commonly utilized in testing General Relativity (GR; e.g. Kramer et al. 2006; Antoniadis et al. 2013). Pulsars are frequently timed for use in Pulsar Timing Arrays (PTAs) due to their stable spin periods (e.g. Hobbs et al. 2010; Manchester et al. 2013) and for probing the nature of the interstellar medium (ISM; Han et al. 2018). While the majority of known pulsars are discovered through periodicity-based searches (Lorimer & Kramer 2012), Rotating Radio Transients (RRATs), a subclass of canonical pulsars, were detected through single-pulse searches instead of the standard Fourier domain searches or conventional folding techniques (McLaughlin et al. 2006; Keane & McLaughlin 2011).

RRATs are notable for their sporadic emissions, with only a few pulses being detected each hour¹ (e.g. Keane et al. 2011). Another intriguing characteristic of RRATs is their similarity in radio emissions to Fast Radio Bursts (FRBs), which are extremely bright and manifest as millisecond-duration burst events. Single-instance RRAT pulses appear indistinguishable from FRB pulses. Dispersion Measure (DM) is used to quantify the time delay caused by the interstellar and intergalactic medium. Generally, FRBs tend to have larger DM values due to their extragalactic origin (Bhandari et al. 2018), while RRATs tend to exhibit relatively lower DM values (Dong et al. 2023). Previous studies have attempted to identify potentially misclassified FRBs as RRATs, especially when they have only been detected through a single-pulse approach (Keane 2016; Rane & Loeb 2016). It has been suggested that magnetars, another subsection of neutron stars with high magnetic fields (Kaspi & Beloborodov 2017), may be responsible for high-energy phenomena such as FRBs (CHIME/FRB Collaboration et al. 2020; Bochenek et al. 2020). Consequently, discovering more RRATs and magnetars can provide insights into the distribution of Galactic pulsars and potentially help characterize the populations of RRATs, FRBs, and magnetars.

RRATs are Galactic pulsars characterized by extremely variable emission of single pulses. They emit individual pulses but then exhibit long periods with no detectable emission. However, only several telescopes with high sensitivity are thought to be suitable to detect such intermittent emissions and obtain sufficient single pulses and periodic emission statistics. This inherent challenge in RRAT detection has resulted in incomplete knowledge regarding the fraction of RRATs that exhibit nulling behavior. Currently, a large number of RRATs lack a precisely measured rotation period, approximately two-thirds have not had their burst rates determined due to a lack of follow-up observations. This lack of data significantly hinders our ability to properly characterize these sources, as highlighted in the study by McKenna et al. (2023). Consequently, in terms of RRATs, it is necessary to conduct long-term monitoring and timing observations.

The sporadic emission mechanism of RRATs remains unknown, primarily due to the inherent difficulties associated with their detection. Despite the discovery of nearly 170 RRATs as of 2023 (e.g. Tyul'bashev et al. 2018; Good et al. 2021), the elusive nature of RRATs has posed significant challenges in unraveling their emission behavior. Since their initial discovery, several models have been put forward to explain these sporadic phenomena. Some examples include: a normal pulsar exhibiting extreme nulling (e.g. Wang et al. 2007; Burke-Spolaor & Bailes 2010), fallback of supernova material (Li 2006), trapped plasma being released from radiation belts (Luo & Melrose 2007), and interference of asteroidal or circumpulsar debris

(Cordes & Shannon 2008). Alternatively, it could be related to mechanisms within the pulsar magnetosphere (e.g. Timokhin 2010; Li et al. 2012; Melrose & Yuen 2014). Efforts have been devoted to understanding this intriguing phenomenon. To establish potential connections between RRATs and normal pulsars, Zhou et al. (2023) conducted an in-depth analysis of 76 Galactic rotating radio transients and their enigmatic emission patterns. The study concluded that RRATs predominantly are weaker pulsars with a few strong pulses or extreme nulling pulsars.

In this paper, we present observations of 10 RRATs conducted at the Parkes 64m radio telescope, utilizing the ultra-wide-bandwidth low-frequency (UWL) receiver, which covers the continuous frequency range of 704-4032 MHz (Hobbs et al. 2020). This receiver system provides unprecedented broadband information, including valuable polarization data, that plays a pivotal role in advancing our understanding of radiation and various phenomena within the intervening interstellar medium (ISM), such as scintillation and dispersion measure (DM) variability (e.g. Karako-Argaman et al. 2015; Heald et al. 2020). Apart from its large fractional bandwidth, it also has a low system temperature, allowing it to operate effectively even in the presence of strong mobile phone transmissions (Hobbs et al. 2020). In recent years, the UWL receiver has played a crucial role in numerous scientific projects related to high-precision pulsar timing, the broadband analysis of pulsar profiles, and the detection of new pulsars and transient sources. Additionally, we analyzed the radiation characteristics of two RRATs observed using other receivers at the Parkes telescope.

2 OBSERVATIONS

A majority of pulsar observations on the Parkes Radio Telescope archive can be obtained at the CSIRO pulsar data archive since 1991. Data sets for a large number of observations will be publicly available after an 18-month embargo² (Hobbs et al. 2011). The observations from the Parkes telescope have been obtained under project codes, mainly P1016 - Instant GRRATification. The RRATs in our sample were observed using the Multibeam, H-OH, 10/50 and UWL receivers (e.g. Manchester et al. 2013; Hobbs et al. 2020). Most of these observations were conducted using the UWL receiver system, with 3328 MHz of bandwidth centered on 2368 MHz and folded in real time into 1024 phase bins. The receiver system provides continuous frequency coverage from 704 to 4032 MHz and has a low temperature (Hobbs et al. 2020). PSRs J1649-4653 and J1709-43 were observed by the Multibeam receiver with 256 MHz of bandwidth divided into 1024 frequency channels and folded in real time into 1024 phase bins. Additionally, the observed bandwidth is normally 512 MHz for the H-OH receiver and 1024 MHz for the 10/50 receiver. All data were recorded with the PSRFITS data format (Hotan et al. 2004). In the observing course, we used 5 backend systems, which included Medusa and the Parkes Digital FilterBank systems (PDFB1,PDFB2,PDFB3, PDFB4; Hobbs et al. 2006).

We investigated 10 RRATs in the CSIRO pulsar data archive and all observation data are publicly available as of 2021. The observing data for the UWL receiver are in search mode, while the data for the H-OH, Multibeam and 10/50 receivers are in fold mode. A summary of the observations is given in Table 1, which lists the fundamental information of the telescope and the project. The search-mode data sets were subsequently folded by DSPSR (van Straten & Bailes 2011), at the rotation period and DM of the RRATs

Table 1: Observing Parameters for 10 RRATs.

PSR	Duration (h)	N_p (pulses)	N_b (pulses)	Burst Rate (h^{-1})	Backend	Frequency (MHz)	Bandwidth (MHz)	Receiver	Mode
J0627+16	0.7	1140	-	-	MEDUSA	2368	3328	UWL	Search
J0628+0909	1.0	3001	61	60	MEDUSA	2368	3328	UWL	Search
J1850+15	0.7	1867	-	-	MEDUSA	2368	3328	UWL	Search
J1909+0641	2.0	9730	116	58	MEDUSA	2368	3328	UWL	Search
J1913+1330	0.9	3459	-	-	MEDUSA	2368	3328	UWL	Search
J1919+1745	1.0	1737	835	847	MEDUSA	2368	3328	UWL	Search
J1928+15	0.3	3012	-	-	MEDUSA	2368	3328	UWL	Search
J1946+24	0.3	257	-	-	MEDUSA	2368	3328	UWL	Search

PSR	Time Span (Years)	Sub-int Length (s)	Backend	Frequency (MHz)	Bandwidth (MHz)	Receiver	Mode
J1649-4653	10.8	10/20/30/60	PDFB1/2/3/4	732/1369/3094	256/1024	H-OH/MULTI/10/50CM	Fold
J1709-43	7.2	10/20/30/50	PDFB3/4	845/1390/3380	64/256/512	H-OH/MULTI/10/50CM	Fold

Notes: We have listed the observing parameters for 10 RRATs, but only PSRs J0628+0909, J1909+0641, J1919+1745 were measured the burst rate. N_p represents the number of total pulses observed, while N_b is the number of burst pulses. The sub-int length represents the sub-integration length.

acquired using PSRCAT (Manchester et al. 2005). The PAZ tool in PSRCHIVE (Hotan et al. 2004) was used to eliminate narrowband and impulsive radio frequency interference (RFI). To further mitigate of potential RFI contamination, we utilized the PFITS_ZAPPROFILE tool in PFITS to process all the data. PFITS is a software package designed for reading, manipulating, and processing PSRFITS format pulsar astronomy data of both search mode and fold mode³. Flux density calibration was made through the observation of the radio galaxy Hydra A (3C 218), where the calibration method can be found in (Liu & Yu 2020). The calibration data are then applied to the RRATs observations using the PAC tool to flatten the bandpass and transform the polarisation products to Stokes parameters. To transform the measured intensities to absolute flux densities, we used PAAS to form noise-free standard templates from observations and then used PSRFLUX to obtain the flux density. In order to obtain the spectral information of RRATs, we divided the frequency bands into several parts and utilized the PULSAR.SPECTRA software to find the best-fitting model and produce publication-quality plots (Swainston et al. 2022).

3 ANALYSIS

3.1 Identification of Single Pulse

The first step in our analysis is to discern the pulses originating from the RRATs. The intermittent nature of RRAT emissions renders Fourier-based techniques or conventional folding search algorithms impractical. Following the method of Xie et al. (2022), we employ the single-pulse search method to specifically target individual pulses surpassing a predefined signal-to-noise ratio (S/N) threshold. Generally, a single-pulse phase can be segmented into two components: the on-pulse region and the off-pulse region. The off-pulse energy is commonly characterized by a Gaussian distribution. We set a minimum detection threshold of

5σ for each pulse, where σ represents the standard deviation of the off-pulse region. To filter out RFI, we exclusively consider pulses whose times of arrival (ToAs) derived from the brightest pulse observed during an observation fall within a 5% deviation from the expected phase. For the purpose of minimizing potential contamination from RFI, each pulse was visually inspected, including an examination of its frequency-phase plots. The total number of detected pulses, the count of filtered pulses and the burst rates for all our target RRATs are listed in Table 1. We only detected single-pulses in 3 RRATs (PSRs J1919+1745, J1909+0641 and J0628+0909).

The integrated profiles of the entire observations for these 3 RRATs are shown in upper panel of Figure 1, in which the on-pulse and off-pulse regions are shown in filled blue and gray areas, respectively. In the lower panel of Figure 1, we showed single-pulse stack of 15 single pulses for each RRAT, in which the burst pulses are labeled in red solid line. It is clear to see that all of these 3 RRATs exhibit sporadic emissions. The burst rate of PSR J1919+1745 is $847 h^{-1}$, which is much larger than that of both PSR J0628+0909 with burst rate of $60 h^{-1}$ and PSR J1909+0641 with burst rate of $58 h^{-1}$.

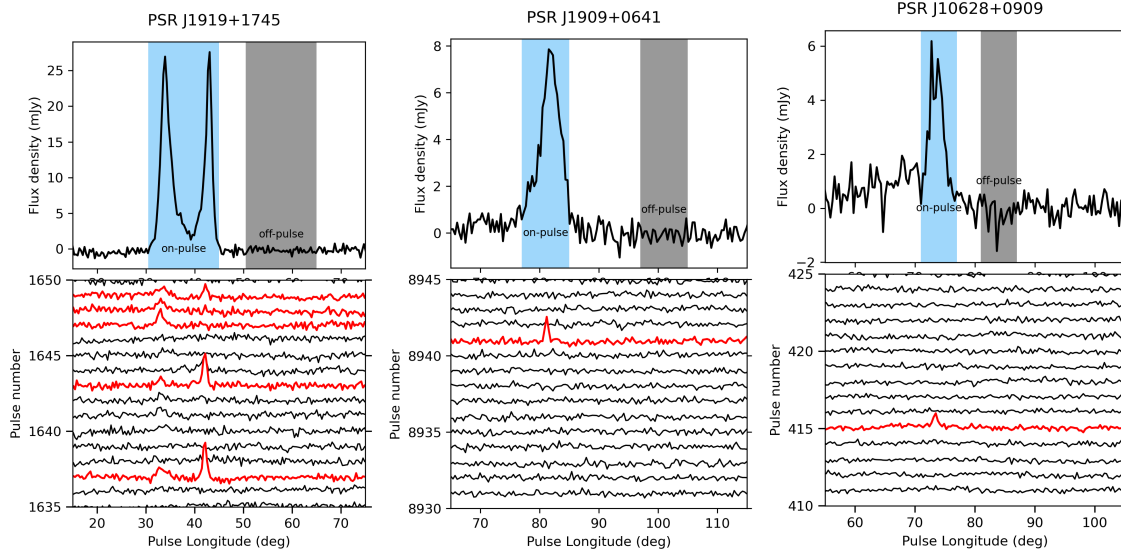


Fig. 1: Integrated profiles and partial pulse sequences of 3 RRATs.

3.2 Profile

Flux calibration procedure was applied to all of the observational data. For the search-mode data, we conducted observations on each RRAT either once or twice, with each observation lasting approximately one hour. To manage individual file sizes, the data was automatically divided into multiple files. We utilized all observation files to generate a cumulative pulse profile, aiming to enhance the signal-to-noise ratio. For the fold-mode data, our analysis focused only on the integrated profile of PSR J1709-43. The sub-integration lengths across 103 observations varied between 10, 20, 30, or 50. To analyze the frequency-dependent characteristics of the integrated pulse profile, we utilized single observational data acquired from three

pulse profiles were observed across all the sub-integrations. Therefore, the sub-integration length across observations did not exert an significant influence on the integrated profile.

3.3 Flux Density Measurements and Spectral Properties

We utilized the PULSAR_SPECTRA software package developed by Swainston et al. (2022), which uses the robust statistical techniques to decide on the optimal fitting model and calculate the corresponding spectral parameters. The publicly available software package presents a comprehensive array of tools dedicated to the systematic cataloging of pulsar flux density and automated spectral fitting. The use of this software facilitates the identification of the most appropriate spectral model. Notably, the PYTHON-based software implements the 5 spectral models, including the Simple power law, Broken power law, Log-parabolic spectrum, Power law with high-frequency cut-off, and Power law with low-frequency turnover. They are adequate for describing the spectra of the vast majority of pulsars, with the simple and broken power-law models being the most widely employed. Although these models are morphological, the spectral index may potentially be associated with other parameters of pulsars. The spectral fitting routine implements the method illustrated in Jankowski et al. (2018). To compare the 5 models, the Akaike information criterion (AIC) was used as a comparison metric, evaluating how much information the model maintains about the data without overfitting. The model leading to the lowest AIC is considered the most accurate in describing the pulsar’s spectra. A more comprehensive description of how to use the PULSAR_SPECTRA software package can be found in Swainston et al. (2022). We presented the results of spectral fitting from integrated pulses of several RRATs. Furthermore, we applied a similar spectral analysis procedure to individual pulses with high signal-to-noise ratio.

4 RESULTS

4.1 Search-mode data

The radio emission from pulsars is affected by propagation through the ISM in both frequency and time domains, spanning durations from seconds to several hours. This phenomenon is recognized as diffractive scintillation. We estimate the scattering time, τ_s at a reference frequency of 1400 MHz using the empirical relationship to DM acquired by Kumamoto et al. (2021):

$$\tau_s = 1.2 \times 10^{-5} DM^{2.2} (1.0 + 0.00194 DM^2). \quad (1)$$

For the wide frequency band of the UWL receiver, we applied the typical relation $\tau_\nu \propto \nu^{-4}$ (Komesaroff et al. 1972) to estimate the scattering time at 950 MHz and 3500 MHz.

The value of scintillation bandwidth in MHz, $\Delta\nu_d$, is given by Cordes & Rickett (1998) as:

$$\Delta\nu_d = \frac{1.16}{2\pi\tau_s}. \quad (2)$$

We estimated the scintillation bandwidth for 3 RRATs at frequencies of 950 MHz, 1400 MHz, and 3500 MHz, as shown in Table 2. The entire observation bandwidth was divided into several sub-bands. For PSRs J1919+1745 and J0628+0909, the minimum bandwidth of each sub-band is 100 MHz, while for PSR

J0628+0909 are all significantly smaller than the minimum bandwidth of each corresponding sub-band. Therefore, the impact of scintillation effects on flux density is deemed negligible in this study.

Table 2: Scintillation bandwidth and minimum sub-band bandwidth of 3 RRATs.

PSR	DM (pc cm^{-3})	$\Delta\nu_{min}$ (MHz)	$\Delta\nu_{950}$ (MHz)	$\Delta\nu_{1400}$ (MHz)	$\Delta\nu_{3500}$ (MHz)
J1919+1745	142.3	100	0.001	0.007	0.3
J1909+0641	36.7	200	0.3	1.5	58.6
J0628+0909	88.3	100	0.01	0.05	2.0

Notes: We have listed the observing parameters for PSRs J1919+1745, J1909+0641, J0628+0909. $\Delta\nu_{min}$ is the minimum channel bandwidth. $\Delta\nu_{950}$, $\Delta\nu_{1400}$, and $\Delta\nu_{3500}$ are the scintillation bandwidth response to 950 MHz, 1400 MHz, 3500 MHz, respectively (Komesaroff et al. 1972).

4.1.1 PSR J1919+1745

We have obtained 835 burst pulses, constituting approximately 48% of all detected single pulses. In Figure 2, we present the integrated profiles of the entire frequency band using 62 observations as well as those of nine sub-bands.

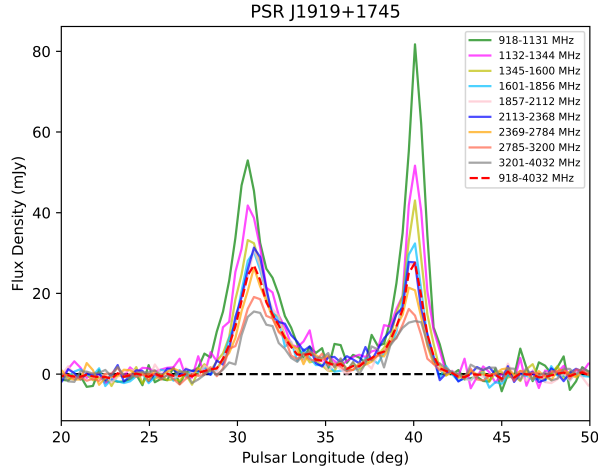


Fig. 2: Integrated profiles of PSR J1919+1745 across 9 frequency sub-bands.

It is evident that all profiles exhibit narrow double-peak characteristics. The width of the observed pulses is 0.6 ms, and it shows negligible variation with a changing frequency. The peak flux densities of the two components of the total integrated profile are similar. At lower frequencies (918-1600 MHz), the latter component dominates. At middle frequencies (1601-2368 MHz), the flux densities of both peaks are similar. Towards the higher frequencies (2369-4032 MHz), the earlier component shows a slightly larger peak flux density. Furthermore, the flux densities of both peaks exhibit a decreasing trend as the frequency increases. Using the method described in Section 3.3, we found that the spectra of both the integrated and individual pulses can be characterized by a simple power law, which takes the following form:

$$S(\nu) = S_0 (\nu/\nu_0)^{-\alpha} \quad (2)$$

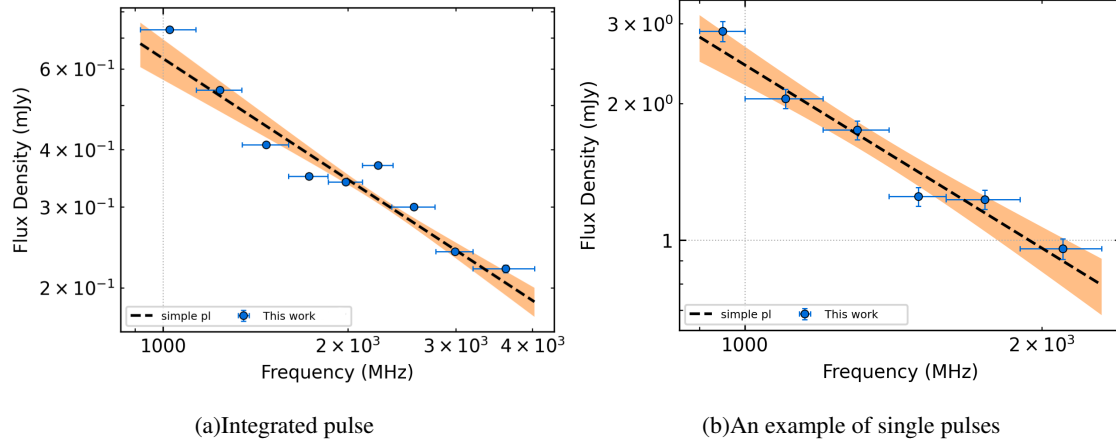


Fig. 3: Spectral of PSR J1919+1745.

where α is the spectral index, ν_0 is the center frequency and c is a constant.

Figure 3 (a) shows that the spectral index of the integrated pulses is -0.9 , which is flatter compared to the average spectral index of most pulsars (-1.60 ± 0.03 , Jankowski et al. 2018). A spectral fitting analysis was conducted on a sample consisting of 49 individual pulses with high signal-to-noise ratios, and all the results followed the simple power law. The average spectral index of 49 single pulses is -1.0 , ranging from -3.5 to 0.01 . An example of single-pulse spectrum is shown in Figure 3 (b).

4.1.2 PSR J1909+0641

During the observation period of 2 hours, we identified 116 burst pulses, corresponding to a burst rate of $58 h^{-1}$. The integrated profiles, encompassing the entire frequency band and six sub-bands, exhibit a distinct

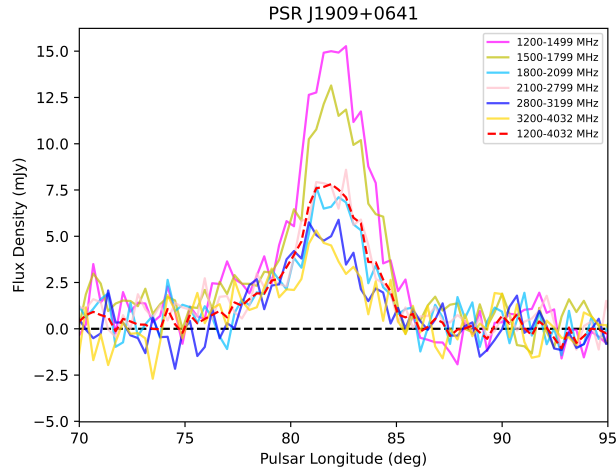


Fig. 4: Integrated profiles of J1909+0641 across 6 frequency sub-bands.

narrow feature, as depicted in Figure 4. The pulse width across various frequency bands is ~ 0.08 ms, and the peak flux density aligns with the general trend of decreasing with increasing frequency.

We performed spectral analysis on the integrated pulse as well as on seven distinct single pulses. It is

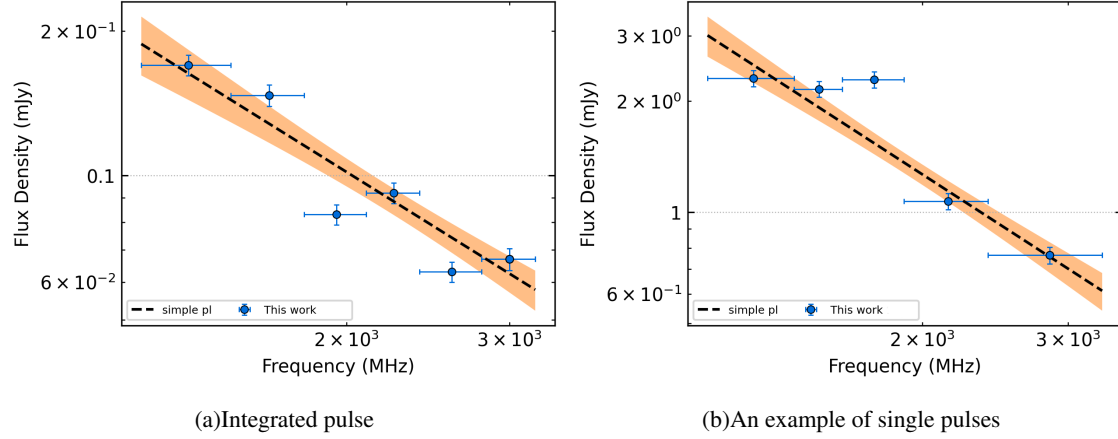


Fig. 5: Spectral of PSR J1909+0641.

index of the integrated pulse is -1.2 , which is relatively flatter compared to the average spectral index of pulsars. Furthermore, the average spectral index of individual pulses is nearly -1.0 , spanning from -1.5 to 0.05 , as presented in Figure 5 (b).

4.1.3 PSR J0628+0909

We detected 61 individual pulses in 1 hour, corresponding to a burst rate of $60 h^{-1}$. The pulse width is 0.11 ms. The data are split into 7 sub-bands. We injected the flux densities of the 7 sub-bands into the PULSAR_SPECTRA flux density catalogue. The spectrum of integrated pulse can be characterized as a simple power law with a spectral index of -1.3 , which is relatively flatter than the average spectral index of normal pulsars. Furthermore, we implemented spectral fitting on 22 high signal-to-noise ratio single pulses using

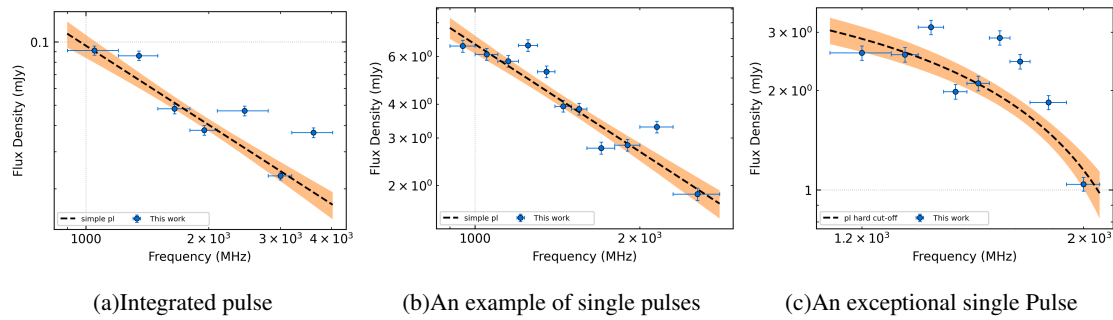


Fig. 6: Spectral of PSR J0628+0909.

the same approach. The vast majority of the single pulse spectrum also follows a simple power law, as presented in Figure 6 (a)(b), with an average spectral index of -1.0 and a range of -1.9 to 0.5 . Notably, there is an intriguing single pulse which can be divided into 11 sub-bands, and its spectrum can be modeled as a high-frequency cut-off power law, as shown in Figure 6 (c), which takes the form:

$$S_\nu = c \left(\frac{\nu}{\nu_0} \right)^\alpha \left(1 - \frac{\nu}{\nu_c} \right), \nu < \nu_c, \quad (4)$$

where α is the spectral index, ν_c is the cut-off frequency and c is a constant. This model exhibits a spectrum steepening or interruption at high frequencies. A possible explanation suggests that radiation originates

star's surface. In this process, electron acceleration reaches a maximum and decreases to zero as their velocity approaches the speed of light. All emitted power is concentrated within the radio frequency band (Kontorovich & Flanchik 2013).

4.1.4 The other RRATs with search mode

For the rest of RRATs observed with the UWL receiver, we could not create reliable profiles. Therefore, we are unable to carry out subsequent processing and analysis, as we have done for the previous three RRATs.

Limits on the flux density of a single pulse can be described by the equation (Tang et al. 2021):

$$S_{lim} = \frac{\sigma S/N_{min} T_{sys}}{G \sqrt{\Delta\nu N_p t_{obs}}}, \quad (5)$$

where $T_{sys}=22$ K is the system temperature, $G=1.8$ K Jy^{-1} is the antenna gain for the UWL receiver of Parkes telescope, t_{obs} is the observation time, σ is the root-mean-square (rms) noise level and $\Delta\nu$ is the full 3300 MHz bandwidth. As for periodic signals, equation 5 should be multiplied by $\sqrt{\frac{\delta}{1-\delta}}$, where δ is the duty cycle. Due to the absence of a measured pulse width for PSR J1850+15 in previous investigations, we assume the pulse width to be 1 ms and a flat spectrum, our non-detection of signal with S/N above 7 puts a fluence limitation of ~ 13 mJy ms. Detailed parameters regarding the limitation of flux density and fluence for the 5 RRATs are listed in Table 3.

Table 3: Summary of the flux density and fluence limits of the single pulses and periodicity search of 5 RRATs with Parkes UWL receiver.

PSR Name	Period (s)	T_{obs} (s)	σ (rms)	Assuming Width Single Pulses(ms)	Width Periodic Signal	Flux Density Limit (7σ) Single Pulse/Periodic Signal	Fluence Limit (7σ) Single Pulse/Periodic Signal
J0627+16	2.2	2442	30.0	0.03	0.3	21.4mJy/7.5 μ Jy	0.6mJy ms/2.3 μ Jy ms
J1913+1330	0.9	3168	34.7	0.2	2.0	38.0mJy/30.2 μ Jy	7.6mJy ms/60.4 μ Jy ms
J1928+15	0.4	1210	12.6	0.5	5.0	21.0mJy/42.9 μ Jy	10.5mJy ms/214.5 μ Jy ms
J1946+24	4.7	1166	21.8	0.4	4.0	10.6mJy/19.6 μ Jy	4.2mJy ms/78.3 μ Jy ms
J1850+15	1.4	2554	32.4	0.1	1.0	29.0mJy/18.1 μ Jy	2.9mJy ms/18.1 μ Jy ms

Notes: The pulse widths for the periodic signals of PSRs J0627+16, J1913+1330, J1928+15, and J1946+24 are from Deneva et al. (2009) and McLaughlin et al. (2009). As for PSR J1850+15, its pulse width was not found in previous works. Therefore, it is assumed to be 1 ms. Additionally, it is assumed that the pulse widths of all individual pulses are one-tenth of the pulse width of periodic pulses.

4.2 Fold-mode data

4.2.1 PSR J1709-43

We collected observational data spanning 7.2 years, from MJD 55537 to 58168. A total of 103 observations were conducted, all in a folded mode. Pulse profiles were detected in 41 observations, constituting $\sim 40\%$ of the overall data set. The majority exhibits continuous pulse signals across all sub-integrations, while only 7 observations experienced nulling. Notably, the highest detection rate was obtained at 1400 MHz, accounting for $\sim 56\%$ of the observations. Three total intensity pulse profiles of PSR J1709-43 at 732 MHz, 1369 MHz, and 3094 MHz are in good agreement which exhibit a narrow single-peaked structure, as presented in Figure

In addition to the analysis presented in Section 3, we performed a timing analysis for PSR J1709-43, which enabled us to determine its rotating period and the first derivative of the rotating period. The full timing solutions are listed in Table 4.

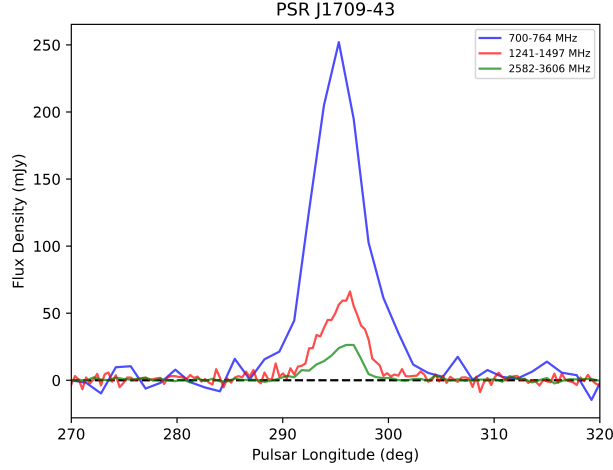


Fig. 7: Integrated profiles of PSR J1709-43 across 3 frequency sub-bands.

Table 4: Ephemeris for PSR J1709-43.

Parameter	Value
Pulsar Name	PSR J1709-43
Right Ascension (RA, J2000)	17:09:46
Declination (Dec, J2000)	-43:54:32
Reference epoch (PEPOCH, MJD)	56800
Data Span (MJD)	55537-58168
Dispersion measure (DM)	228 pc cm ⁻³
Rotation frequency (F_0)	1.1149999997 Hz
Frequency derivative (F_1)	$-3.0038 \times 10^{-14} \text{ s}^{-2}$
Rotation period (P_0)	0.8968609868 s
Period derivative (P_1)	$2.4162 \times 10^{-14} \text{ ss}^{-1}$
Surface magnetic field (B_s)	$4.71 \times 10^{12} \text{ G}$
Characteristic age (τ)	0.59 Myr

4.2.2 PSR J1649-4653

Similar to PSR J1709-43, we have collected data for PSR J1649-4653 covering 11 years, from MJD 54220 to 58222, with a total observation time of 10 hours. All the observations were carried out in the folded mode. Out of these, 65 observations ($\sim 51\%$) detected the burst pulse profiles. Figure 7 illustrates the variation of peak flux density of J1649-4653 with time. The flux density of PSR J1649-4653 is found to be significantly

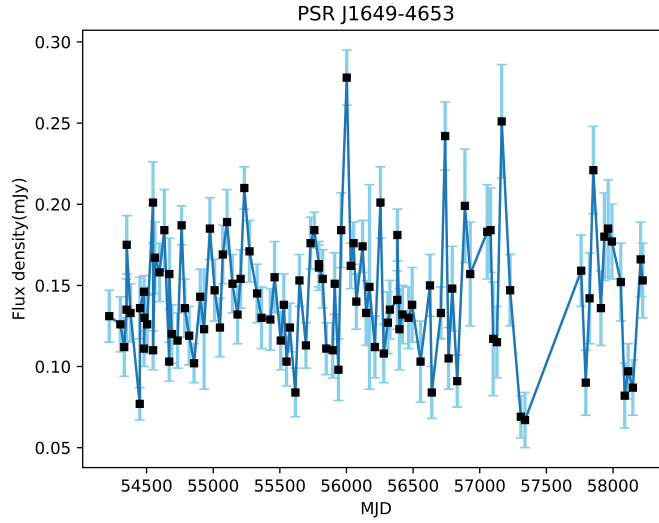


Fig. 8: Flux density as a function of MJD for PSR J1649-4653.

5 DISCUSSION

We calculated the burst rates for three RRATs, PSRs J1919+1745, J1909+0641, and J0628+0909. These rates were then compared with results from the Arecibo telescope (Deneva et al. 2009) and the Five-hundred-meter Aperture Spherical radio Telescope (FAST, Hsu et al. 2023), as detailed in Table 5. Notably, J1919+1745 exhibited outstanding behavior with an observed burst rate of $847 h^{-1}$, which significantly exceeds the previously reported rate of $320 h^{-1}$ from the Arecibo Telescope. Furthermore, the burst pulses constituted $\sim 50\%$ of all the observed individual pulses. Consequently, we suggest that PSR J1919+1745 may be reclassified from a RRAT to a nulling pulsar. For PSR J1909+0641, the observed burst rate was $58 h^{-1}$, relatively lower than the rate of $67 h^{-1}$ observed at Arecibo telescope. For PSR J0628+0909, the burst rate observed in this study was $60 h^{-1}$. In comparison, the Arecibo reported a rate of $141 h^{-1}$ ($S/N > 5$), and the FAST reported a rate of $270 h^{-1}$ ($S/N > 7$). We collected data from 103 observations for PSR J1709-43 in fold mode. Among these, pulse profiles is detected in 41 observations ($\sim 40\%$). Pulse signals can be seen across all sub-integrations for most of them, with only 7 observations experiencing nulling. 128 observations were collected for PSR J1649-4653 in fold mode, pulse emissions were detected for approximately 51% (65 observations). Our analysis suggests that the variations in burst rates can be attributed to three primary factors. Firstly, variations in telescope sensitivity and observation bandwidth play a vital role. If telescopes with higher signal-to-noise ratios are employed for observations, it is possible that a greater number of burst pulses could be detected. The different burst rates observed in PSR J0628+0909 may be attributed to the sensitivity of different telescopes. The FAST telescope demonstrates the highest sensitivity, corresponding to the highest burst rate. Secondly, variations in the duration of observations can exert an influence. The observation durations of the FAST and the Arecibo telescopes were comparatively shorter than that of the Parkes telescope. Lastly, it is worth noting that the burst rates of RRATs may exhibit temporal evolution.

We analyzed the integrated profiles spanning multiple frequency sub-bands for PSRs J1919+1745, J1909+0641, and J1709-43. A notable trend was discerned: the peak flux densities exhibited a diminishing

Table 5: Comparison of burst rates detected of three telescopes.

PSR	Burst Rate			Frequency			Duration		
	Parkes (h^{-1})	Arecibo (h^{-1})	FAST (h^{-1})	Parkes (MHz)	Arecibo (MHz)	FAST (MHz)	Parkes (h)	Arecibo (h)	FAST (h)
J1919+1745	847	320	–	732-4032	1390-1490	–	1.0	0.11	–
J1909+0641	58	67	–	732-4032	1390-1490	–	2.0	0.15	–
J0628+0909	60	141	270	732-4032	1390-1490	1000-1500	1.0	0.30	0.48

Notes: The observational data in this study were acquired using the Parkes telescope. The Arecibo data were sourced from Deneva et al. (2009), while the FAST data were obtained from Hsu et al. (2023).

Subsequently, we carried out an analysis and fitting of the flux density in various frequency sub-bands for both integrated and single pulses. This analysis was facilitated using an automated spectral fitting software, PULSAR_SPECTRA. We present the spectral analyses of the integrated pulses emanating from three RRATs, PSRs J1919+1745, J1909+0641, and J0628+0909. All of them consistently follow a simple power law. The integrated results are consistent with previous work, which presented that 79% of pulsars have spectra with a simple power law (Jankowski et al. 2018).

However, there is a dearth of literature available for comparing single-pulse spectral index with our results. It’s remarkable that only one single-pulse spectral fitting of PSR J0628+0909 exhibits a high-frequency cut-off power-law spectrum with a cut-off at 1625 MHz. Complex spectral fitting typically requires a substantial number of flux density at different frequencies. However, our current limitations lie in acquiring a significant volume of high-quality single-pulse spectral flux density data. This may lead to a predominant trend in our fitting results, favoring a simple power-law model. Jankowski et al. (2018) summarized that there are 3 scenarios for deviations from a simple power-law model in pulsars can be considered: an environmental origin of the observed spectral features, absorption processes in the magnetosphere, and non-generic emission characteristics. The calculated mean of the single-pulse average spectral indices for the aforementioned three RRATs, as presented in Table 6. Nevertheless, there is a dearth of literature avail-

Table 6: Spectral indices of 3 RRATs

PSR	Integrated Pulse	Single Pulse		
		Mean	Standard Deviation	Range
J1919+1745	-0.9	-1.0	1.0	-3.5 - 0.2
J1909+0641	-1.2	-1.0	0.5	-1.5 - 0.05
J0628+0909	-1.0	-1.3	0.7	-2.0 - 0.5

able for comparing single-pulse spectral indices with our results. Previous studies by Shapiro-Albert et al. (2018) reported that the mean spectral indices for PSRs J1819-1458, J1317-5759, and J1913+1330 are -1.1, -0.6, and -1.2 respectively. The range of single-pulse spectral indices they obtained is from -7 to +4. Xie et al. (2022) reported that the mean spectral index for single pulses is -3.2 for PSR J0139+3336 and showed an extensive range from -11.85 to +3.83. The frequency ranges for these two observations were relatively narrow, spanning 288 MHz and 500 MHz, respectively. Meyers et al. (2019) reported that the single-pulse mean spectral index for PSR J2335-0530 is -2.2, ranging from -2.8 to -1.5. The observational data were

other centered at 1396MHz with a bandwidth of 256MHz. Consequently, the observation covered a broad frequency range. Our results exhibit relatively lower scatter compared to the results from Shapiro-Albert et al. (2018) and Xie et al. (2022), which may be attributed to the broader frequency range we measured (3300 MHz) and the longer observation duration.

6 SUMMARY

We performed an analysis of the emission properties for 10 RRATs, obtaining burst rates for 3 RRATs and integrated profiles across multiple frequency bands for 3 RRATs. We also conducted an in-depth wide-band analysis of the integrated pulse and single-pulse spectral characteristics using the PULSAR_SPECTRA software package. Our findings indicate that the vast majority of these characteristics align with a simple power-law model, featuring relatively flat spectral indices and a comparatively small scatter in single-pulse spectral indices. For five additional RRATs observed with the UWL receiver, we provide their fluence and flux density upper limits. Furthermore, we derived the timing solution for PSR J1709-43. Based on the classification of 76 recently discovered RRATs by the FAST telescope in the previous work of Zhou et al. (2023), we suggest that PSRs J1919+1745, J1709-43 and J1649-465 may be nulling pulsars or weak pulsars with sparse strong pulses.

Acknowledgements The Parkes radio telescope is part of the Australia Telescope National Facility, which is funded by the Australian Government funds operation as a National Facility managed by CSIRO. This paper includes archived data obtained through the CSIRO Data Access Portal ⁴. This work is supported by the Major Science and Technology Program of Xinjiang Uygur Autonomous Region (grant no. 2022A03013-4), the Zhejiang Provincial Natural Science Foundation of China (grant no. LY23A030001), the National SKA Program of China (grant no. 2020SKA0120100, 2022YFC2205201, 2020SKA0120200), the Natural Science Foundation of Xinjiang Uygur Autonomous Region (grant no. 2022D01D85), the National Natural Science Foundation of China (grant no. 12041304, 12273100, 12041303), and the West Light Foundation of Chinese Academy of Sciences (grant no. WLFC 2021-XBQNXZ-027), and the open program of the Key Laboratory of Xinjiang Uygur Autonomous Region (grant no. 2020D04049).

References

- Antoniadis, J., Freire, P. C. C., Wex, N., et al. 2013, *Science*, 340, 448 2
- Bhandari, S., Keane, E. F., Barr, E. D., et al. 2018, *MNRAS*, 475, 1427 2
- Bochenek, C. D., Ravi, V., Belov, K. V., et al. 2020, *Nature*, 587, 59 2
- Burke-Spolaor, S., & Bailes, M. 2010, *MNRAS*, 402, 855 2
- CHIME/FRB Collaboration, Andersen, B. C., Bandura, K. M., et al. 2020, *Nature*, 587, 54 2
- Cordes, J. M., & Rickett, B. J. 1998, *ApJ*, 507, 846 6
- Cordes, J. M., & Shannon, R. M. 2008, *ApJ*, 682, 1152 3
- Deneva, J. S., Cordes, J. M., McLaughlin, M. A., et al. 2009, *ApJ*, 703, 2259 10, 12, 13
- Dong, F. A., Crowter, K., Meyers, B. W., et al. 2023, *MNRAS*, 524, 5132 2
- Good, D. C., Andersen, B. C., Chawla, P., et al. 2021, *ApJ*, 922, 43 2

- Han, J. L., Manchester, R. N., van Straten, W., & Demorest, P. 2018, *ApJS*, 234, 11 2
- Heald, G., Mao, S., Vacca, V., et al. 2020, *Galaxies*, 8, 53 3
- Hobbs, G. B., Edwards, R. T., & Manchester, R. N. 2006, *MNRAS*, 369, 655 3
- Hobbs, G., Archibald, A., Arzoumanian, Z., et al. 2010, *Classical and Quantum Gravity*, 27, 084013 2
- Hobbs, G., Miller, D., Manchester, R. N., et al. 2011, *PASA*, 28, 202 3
- Hobbs, G., Manchester, R. N., Dunning, A., et al. 2020, *PASA*, 37, e012 3
- Hotan, A. W., van Straten, W., & Manchester, R. N. 2004, *PASA*, 21, 302 3, 4
- Hsu, J. A., Jiang, J. C., Xu, H., Lee, K. J., & Xu, R. X. 2023, *MNRAS*, 518, 1418 12, 13
- Jankowski, F., van Straten, W., Keane, E. F., et al. 2018, *MNRAS*, 473, 4436 6, 8, 13
- Karako-Argaman, C., Kaspi, V. M., Lynch, R. S., et al. 2015, *ApJ*, 809, 67 3
- Kaspi, V. M., & Beloborodov, A. M. 2017, *ARA&A*, 55, 261 2
- Keane, E. F. 2016, *MNRAS*, 459, 1360 2
- Keane, E. F., Kramer, M., Lyne, A. G., Stappers, B. W., & McLaughlin, M. A. 2011, *MNRAS*, 415, 3065 2
- Keane, E. F., & McLaughlin, M. A. 2011, *Bulletin of the Astronomical Society of India*, 39, 333 2
- Komesaroff, M. M., Hamilton, P. A., & Ables, J. G. 1972, *Australian Journal of Physics*, 25, 759 6, 7
- Kontorovich, V. M., & Flanchik, A. B. 2013, *Ap&SS*, 345, 169 10
- Kramer, M., Stairs, I. H., Manchester, R. N., et al. 2006, *Science*, 314, 97 2
- Kumamoto, H., Dai, S., Johnston, S., et al. 2021, *MNRAS*, 501, 4490 6
- Li, J., Spitkovsky, A., & Tchekhovskoy, A. 2012, *ApJ*, 746, L24 3
- Li, X.-D. 2006, *ApJ*, 646, L139 2
- Liu, B., & Yu, S. 2020, in *Big Data in Astronomy: Scientific Data Processing for Advanced Radio Telescopes*, ed. L. Kong, T. Huang, Y. Zhu, & S. Yu, 165 4
- Lorimer, D. R., & Kramer, M. 2012, *Handbook of Pulsar Astronomy* 2
- Luo, Q., & Melrose, D. 2007, *MNRAS*, 378, 1481 2
- Manchester, R. N., Hobbs, G. B., Teoh, A., & Hobbs, M. 2005, *AJ*, 129, 1993 4
- Manchester, R. N., Hobbs, G., Bailes, M., et al. 2013, *PASA*, 30, e017 2, 3
- McKenna, D. J., Keane, E. F., Gallagher, P. T., & McCauley, J. 2023, *arXiv e-prints*, arXiv:2302.12661 2
- McLaughlin, M. A., Lyne, A. G., Lorimer, D. R., et al. 2006, *Nature*, 439, 817 2
- McLaughlin, M. A., Lyne, A. G., Keane, E. F., et al. 2009, *MNRAS*, 400, 1431 10
- Melrose, D. B., & Yuen, R. 2014, *MNRAS*, 437, 262 3
- Meyers, B. W., Tremblay, S. E., Bhat, N. D. R., et al. 2019, *PASA*, 36, e034 13
- Rane, A., & Loeb, A. 2016, *arXiv e-prints*, arXiv:1608.06952 2
- Shapiro-Albert, B. J., McLaughlin, M. A., & Keane, E. F. 2018, *ApJ*, 866, 152 1, 13, 14
- Swainston, N. A., Lee, C. P., McSweeney, S. J., & Bhat, N. D. R. 2022, *PASA*, 39, e056 4, 6
- Tang, Z., Zhang, S., Dai, S., Li, Y., & Wu, X. 2021, *arXiv e-prints*, arXiv:2106.04821 10
- Timokhin, A. N. 2010, *MNRAS*, 408, L41 3
- Tyul'bashev, S. A., Tyul'bashev, V. S., & Malofeev, V. M. 2018, *A&A*, 618, A70 2
- van Straten, W., & Bailes, M. 2011, *PASA*, 28, 1 3
- Wang, N., Manchester, R. N., & Johnston, S. 2007, *MNRAS*, 377, 1383 2

Xie, J., Wang, J., Wang, N., et al. 2022, *ApJ*, 940, L21 1, 4, 13, 14

Zhou, D. J., Han, J. L., Xu, J., et al. 2023, *arXiv e-prints*, [arXiv:2303.17279](https://arxiv.org/abs/2303.17279) 3, 14